Available online at www.sciencedirect.com
SCIENCE DIRECT®
International Journal of Heat and Mass Transfer 48 (2005) 4854–4866
International Journal of HEAT and MASS TRANSFER
www.elsevier.com/locate/ijhmt

Numerical study of swirling flows in a cylindrical container with co-/counter-rotating end disks under stable temperature difference

Yuka Omi, Reima Iwatsu *

Tokyo Denki University, 2-2 Kanda-Nishiki-cho, Chiyoda-ku, Tokyo 101-8457, Japan

Received 13 February 2004; received in revised form 27 April 2005
Available online 26 August 2005

Abstract

A numerical study was conducted to investigate swirling flows of a Boussinesq fluid confined in a cylindrical container with co-/counter-rotating end disks. A vertically stable temperature gradient is imposed, with the stationary sidewall assumed as adiabatic. Flows are studied for a range of parameters: the Reynolds number, Re, $100 \leqslant Re \leqslant 2000$; the Richardson number, Ri, $0 \leqslant Ri \leqslant 1.0$; and the Prandtl number, Pr, $Pr = 1.0$. The ratio of the angular velocity of the top disk to the bottom disk, s, $-1.0 \leqslant s \leqslant 1.0$. The cylinder aspect ratio: $h = 2.0$. For the case of negligibly small temperature difference ($Ri \sim 0$) and high Re, interior fluid rotates with an intermediate angular velocity of both end disks when they are co-rotating ($s > 0$). When end disks are counter-rotating ($s < 0$), shearing flow with meridional recirculation is created. For the case of large temperature difference ($Pr \cdot Ri \sim \mathrm{O}(1)$), the Ekman suction is suppressed and the sidewall boundary layer disappears at mid-height of the cylinder. For all the values of s considered in the present study, the bulk of the fluid is brought close to rest with the fluid in the vicinity of both end disks rotating in each direction. The secondary flow in the meridional section of the cylindrical container exhibits various types of vortices as the governing parameters are varied. These flow patterns are presented in the form of diagrams on the (s, Re) plane and (s, Ri) plane. The average Nusselt number is computed and presented as functions of Ri, Re and s.

1. Introduction

The flow of fluid layer between two rotating disks has provided fertile research topics for theorists [1–6]. The confined swirling flow has relevance also to many technological applications, e.g., rotating machinery, thrust bearings, viscometry, computer storage devices and material processing units [7,8]. It is known that the rotating flow over a disk of infinite expanse can be solved analytically by assuming the similarity solution [1]. By applying the von Kármán similarity transformation, the partial differential equations are decomposed into a system of ordinary differential equations for four unknowns. Similarity transformation was applied to the flow between two infinite disks by Batchelor [2] and Stewartson [3]. Analytical solutions derived by these two authors exhibit qualitatively different behavior at the limit of high Reynolds number [4]. If we assume the angular velocity of the top and bottom disks as Ω_s and Ω, respectively, the Batchelor solution predicts that in

* Corresponding author. Tel.: +81 3 5280 3373; fax: +81 3 5280 3568.
E-mail address: iwatsu@cck.dendai.ac.jp (R. Iwatsu).

0017-9310/$ - see front matter © 2005 Elsevier Ltd. All rights reserved.
doi:10.1016/j.ijheatmasstransfer.2005.05.038

Nomenclature

Ek	Ekman number ($Ek = \nu/\Omega R^2$)
Gr	Grashof number ($Gr = g\alpha\Delta T R^3/\nu^2$)
g	gravity acceleration
H	height of the cylindrical container
h	cylinder aspect ratio ($h = H/R$)
N	Brunt Väisälä frequency ($N = (g\alpha\Delta T/H)^{1/2}$)
Nu	local Nusselt number $\left(Nu(r) = \frac{\partial T}{\partial z}\big\|_{z=0 \text{ or } z=h}\right)$
$\overline{Nu}$	average Nusselt number $\left(\overline{Nu} = \frac{1}{\pi}\int_0^{2\pi}\int_0^1 \frac{\partial T}{\partial z} r\,\mathrm{d}r\,\mathrm{d}\theta\right)$
Pr	Prandtl number ($Pr = \nu/\kappa$)
R	radius of the cylindrical container
Re	Reynolds number ($Re = \Omega R^2/\nu$)
Ri	Richardson number ($Ri = Gr/Re^2 = \alpha g\Delta T/\Omega^2 R$)
Ro	Rossby number ($Ro = 1 - s$)
r	radial coordinate
S	stratification parameter ($S = N^2/\Omega^2$)
s	ratio of the angular velocity of top disk to bottom disk ($s = \Omega_s/\Omega$)
T	temperature
T_0	average temperature
u	radial velocity component
v	azimuthal velocity component
w	axial velocity component
z	axial coordinate
α	thermal expansion coefficient
ΔT	temperature difference between the top and bottom disks
Δt	discrete time increment
κ	thermal diffusion coefficient
ν	kinematic viscosity
φ	azimuthal coordinate
ψ	Stokes streamfunction
Ω	angular velocity of bottom disk
Ω_s	angular velocity of top disk
ω	azimuthal vorticity component

the inviscid limit with $s\,(=\Omega_s/\Omega) = 0$, the bulk fluid rotates at an angular velocity $\gamma\Omega$ $(0 < \gamma < 1)$. The solution by Stewartson on the other hand predicts that the boundary layer is formed only on the rotating bottom disk and the bulk fluid is at rest. Apparently contradictory result deduced from the von Kármán similarity solution has led to intensive theoretical studies and disclosure of non-uniqueness and multiplicity of solutions as the control parameter is varied [4,5]. In more realistic set up of the boundary conditions, i.e., the flows on finite disks, the importance of the sidewall boundary conditions on determining the nature of the inner flow has been recognized [4–6]. For the flows in the cylindrical container with the rotating top disk and co-/counter-rotating sidewall and bottom disk, velocity distribution similar to both Batchelor and Stewartson types is observed depending on the value of the parameters [9]. In the recent studies by Lopez et al. [10,11], transition from steady to unsteady oscillatory flows is investigated for the same cover-casing problem. The linear stability of the steady state solutions with respect to axisymmetric disturbances is analyzed by Gelfgat et al. [12,13] for homogeneous fluid confined in cylinders with co-/counter-rotating top and bottom disks.

In many practical applications, heat transfer is associated with the rotating fluid flows. Considerable amount of previous investigations have directed toward the convection and instabilities in connection with the crystal growth processing units where thermally unstable boundary conditions are imposed (see, e.g., [7,8] and references therein). It appears that a relatively small amount of studies have been done on the laminar rotating flow confined in containers under stable temperature difference. The properties of rotating flow under thermal stratification were theoretically studied by Barcilon and Pedlosky [14,15]. The swirling flow between finite disks under stabilizing temperature difference was numerically studied by Hyun and coworkers [16,17] for sealed cylindrical container when one of the end disks is rotating. The primary objective of their numerical investigation was to elucidate the effect of buoyancy on the emergence of vortex breakdowns. Detailed description of the varied heat transfer and the flow as the stratification parameter and the Reynolds number is given in [18] for the cylinder at a fixed aspect ratio. According to these previous studies on the flows in the cylindrical container with one of the end disks rotating, the inner fluid approaches a state of rest, i.e., the inner fluid does not rotate, and the boundary layer is formed only on the rotating disk at a relatively high Reynolds number under the imposition of large vertical temperature difference. It is of interest to predict the corresponding behavior for the case of flows in a container with both end disks rotating, however, the above flow problem has not attracted much attention in the past. The flows as well as the heat transfer between two finite disks have yet to be analyzed. In the present study, therefore, the swirling flow driven by co-/counter-rotating end disks in a cylindrical container with stationary sidewall is numerically examined for the axisymmetric parameter range. Particular interest is

focused on the behavior of the fluid in the bulk of the cylindrical container under large vertical temperature difference and the heat transfer characteristics as the rotation ratio of the disks s is varied.

2. Mathematical and numerical models

The governing equations are the continuity equation, the Navier–Stokes equations and the energy equation. When the Stokes streamfunction ψ (Eq. (1)) and the azimuthal component of the vorticity ω (Eq. (2)) are introduced, the equations to be solved are the vorticity transport equation (3), the Poisson equation for ψ and ω (Eq. (4)), the azimuthal momentum equation (5), and the energy equation (6).

$$u = -\frac{1}{r}\frac{\partial \psi}{\partial z}, \quad w = \frac{1}{r}\frac{\partial \psi}{\partial r}, \tag{1}$$

$$\omega = \omega_\phi = \frac{\partial u}{\partial z} - \frac{\partial w}{\partial r}, \tag{2}$$

$$\frac{\partial \omega}{\partial t} + \frac{\partial}{\partial r}(u\omega) + \frac{\partial}{\partial z}(w\omega) - \frac{1}{r}\frac{\partial v^2}{\partial z} = \frac{1}{Re}\left[\frac{\partial}{\partial r}\left\{\frac{1}{r}\frac{\partial}{\partial r}(r\omega)\right\} + \frac{\partial^2 \omega}{\partial z^2}\right] - Ri\frac{\partial T}{\partial r}, \tag{3}$$

$$\frac{1}{r}\frac{\partial^2 \psi}{\partial z^2} + \frac{\partial}{\partial r}\left(\frac{1}{r}\frac{\partial \psi}{\partial r}\right) = -\omega, \tag{4}$$

$$\frac{\partial v}{\partial t} + \frac{\partial}{\partial r}(uv) + \frac{\partial}{\partial z}(wv) + \frac{2uv}{r} = \frac{1}{Re}\left[\frac{\partial}{\partial r}\left\{\frac{1}{r}\frac{\partial}{\partial r}(rv)\right\} + \frac{\partial^2 v}{\partial z^2}\right], \tag{5}$$

$$\frac{\partial T}{\partial t} + \frac{\partial}{\partial r}(uT) + \frac{\partial}{\partial z}(wT) + \frac{uT}{r} = \frac{1}{PrRe}\left\{\frac{1}{r}\frac{\partial}{\partial r}\left(r\frac{\partial T}{\partial r}\right) + \frac{\partial^2 T}{\partial z^2}\right\}. \tag{6}$$

These equations in conservation form are spatially discretized by using the second-order central difference schemes on uneven grid points [19]. Time-marching is done by a combination of second-order Adams–Bushforth method and the Crank–Nicolson method. The Poisson equation is iteratively solved by the RB-SOR method. After all the variables are appropriately nondimensionalized, the physical parameters that describe the flows are the Reynolds number $Re = \Omega R^2/v$, the Richardson number $Ri = \alpha g \Delta T/\Omega^2 R$, the Prandtl number $Pr = \kappa/v$, the ratio of the angular velocity of the top disk to the bottom disk $s = \Omega_s/\Omega$ and the cylinder aspect ratio $h = H/R$, where v is the kinematic viscosity, α the thermal expansion coefficient, κ the thermal diffusion coefficient and g the gravity acceleration, respectively. Alternative choices of parameters are possible, e.g., the Ekman number $Ek = v/\Omega R^2$, the Rossby number $Ro = 1 - s$, the Prandtl number Pr, the stratification parameter $S = N^2/\Omega^2$ and the aspect ratio h might be suitable for a certain range of parameters, where $N = (g\alpha\Delta T/H)^{1/2}$ is the Brunt Väisälä frequency.

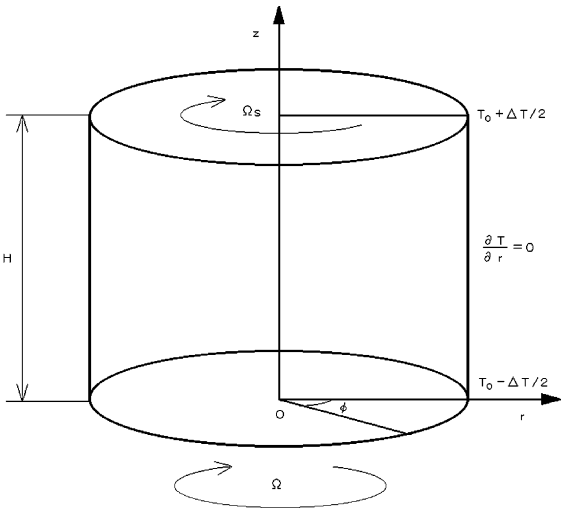

Fig. 1. Boundary conditions and flow configuration.

The boundary conditions and the flow configuration are schematically illustrated in Fig. 1. The angular velocity of the bottom disk is set at $\Omega\,(=-1)$ whereas that of the top disk Ω_s $(=\Omega \cdot s)$ is varied in a range of $-1.0 \leqslant s \leqslant 1.0$. Computations are done for the thermal condition that temperature of the top disk is maintained higher than the bottom disk ($\Delta T \geqslant 0$). The sidewall of the cylinder is assumed to be adiabatic.

The initial condition for each parametric case is that the fluid is at rest when a linear temperature distribution is established in the vertical direction. Top and bottom disks start their rotation with angular velocity Ω_s and Ω, respectively, at time $t = 0$ and time marching is continued until predetermined convergence criterion is satisfied at a large time.

Unevenly spaced grid points are generated by using a hyperbolic tangent function. Prior to the computation, the influence of mesh size was checked at a representative set of physical parameters. The result of this grid dependency check was that the deviation in the maximum value of the streamfunction and the average Nusselt number between the medium grid system with 81×161 points and the fine grid system with 161×321 points is 0.4% and 1.3%, respectively. For these test calculations, the average Nusselt number evaluated at $z = 0$ and $z = h$ coincided up to seven digits. Since these values are considered to exhibit sufficient degree of accuracy for the purpose of the present study, the medium grid system with 81×161 grid points is used in the following computations.

3. Results

Numerical solutions are obtained for $100 \leqslant Re \leqslant 2000$, $0 \leqslant Ri \leqslant 1.0$, $-1.0 \leqslant s \leqslant 1.0$, $Pr = 1.0$ and $h =$

2.0. In the linear stability analysis by Gelfgat et al. [12], the critical Reynolds number Re_{crit} of the flow of homogeneous fluid to axisymmetric disturbances exhibits lowest value ($Re_{crit} = 1646$) at $s = -1$ on the interval $-1 \leqslant s \leqslant 1$ for $h = 1.5$. Similar analysis [13] conducted for flows with co-rotating disks ($s = 1$) indicates that $Re_{crit} = 3845$ at $h = 1.5$ and $Re_{crit} = 2567$ at $h = 2.0$. As the stability limit of inhomogeneous fluid for the present problem is not known from the previous literatures, the value of Re in the present study was arbitrarily chosen so as to study the steady axisymmetric flows. After the computations, cases at high Re, $Ri = 0$ and negative s turned out to be unsteady (see Fig. 3). The values of stability limit obtained in the present study are $Re_{crit} = 1982$ at $s = -0.925$ and $Re_{crit} = 1948$ at $s = -1$. The average Nusselt number for these cases is included in Figs. 12 and 13 because the temporal variation in $\overline{Nu}$ is small. In the following subsections, the results of parametric computation are first presented in the form of a diagram (in Figs. 3 and 4) showing the influence of physical parameters on the creation of meridional flow patterns. Flows are subsequently examined for representative cases of $Re = 1000$ under negligible temperature difference ($Ri = 0$) in Fig. 5 and then under large temperature difference ($Ri = 1.0$) in Fig. 6, respectively. The velocity and the temperature distributions are plotted in Fig. 7 and analyzed in Fig. 8. The Nusselt number is scrutinized in Figs. 9–13.

3.1. Meridional flow pattern

In order to obtain a perspective view over the characteristic features of the flows as Re, Ri and s are varied, diagrams are made in Figs. 3 and 4 that present maps of flow patterns encountered in the course of extensive parametric computations (Fig. 2). The case of negligible temperature difference ($Ri = 0$) is plotted on a separate diagram in Fig. 3 because it deserves particular attention as $Ri = 0$ corresponds to the case of pure forced convection. The case of positive temperature difference ($Ri > 0$) is shown on (s, Ri) plane for $Re = 100$ and 1000 in Fig. 4.

The contour plots of meridional streamfunction showing various shapes of vortices as the rotation ratio is varied were presented in [12,23]. However, the streamline plots in [12] is restricted to limited values of Re and h. Diagram presented by Jahnke and Valentine in [23] which they called cartoon, disregarded many flow types and the information is limited to $s \geqslant -0.1$ since their motivation was mainly to investigate the deformation and changes of vortex breakdown bubbles. Therefore, the result of the present study charted in Fig. 3 offers coherent picture of the secondary flow patterns, to the author's knowledge, for the first time over the entire range of $-1 \leqslant s \leqslant 1$. All the data points plotted in [23] is read from their figure and reproduced by triangles in the diagram. These points indicate the critical values of s and Re at which separation bubbles first occur or transitions to different types of bubbles occur. The corresponding values of the present computation are shown by curves in the diagram. The position of these boundary curves is determined as a midpoint of two points on the parameter plane where solutions are actually computed. Since a large number of computations had been carried out (about 800 cases in Fig. 3 and 1000 cases in Fig. 4), the minimum distance of neighboring points in the diagrams falls down to small values, i.e., $\Delta s = 0.001$, $\Delta Re = 6.25$ ($=100/16$) and $\Delta Ri = 0.0125$ ($=0.1/16$). These small increments of parameters induce practically no need for interpolation method in the present study. The agreement between [23] and the present computation appears to be fair. Other marks distributed in Fig. 3 (and Fig. 4) represent points where flow patterns listed in Fig. 2 are drawn.

The influence of end disk rotation on the flow that contains two axis bubbles was experimentally observed by Roesner [24] and computed by Gelfgat et al. [12]. Gelfgat et al. affirmed that with a weak increase of co-rotation ($s = 0.03$ at $Re = 2000$) two separation bubbles merge and form a relatively large separation vortex bubble. Weak counter-rotation eliminates both bubbles at $s = -0.04$ when $Re = 2000$. In the present diagram, a narrow strip along $s = 0$, $Re \geqslant 1748$ represents the parameter region where two axis vortex bubbles occur (type C_2 flow). This parameter region spans approximately from $s = -0.008$ to $s = 0.02$ at $Re = 2000$ and it is adjacent to the regions for type C and type C_{2m} flows in the negative and positive s directions, respectively. The parameter region for type C flow is then converted into the region for type A flow at $s = -0.04$ and $Re = 2000$ as s is further decreased. In the positive s direction, on increasing the value of s, the parameter region for type C_{2m} flow is varied into the region for type C flow at $s = 0.057$ and $Re = 2000$. Thus, the present result is consistent with the previous studies and presenting the behavior of the separation vortex bubbles in a comprehensive manner.

It might be worth pointing out that the present study reveals minute details about the parameter dependency of counter-rotating ($s < 0$) flow patterns not recognized in the previous studies. For example, type A flow at $s = 0$ is directly deformed into type B flow as s is decreased to a certain negative value when $Re \leqslant 1013$. Deformation is caused by a gradual growth of corner recirculating zone and migration of stagnation point from the top disk to the axis of rotation. Whereas for $Re \geqslant 1263$, separation occurs on the top disk (type A_0 flow) in a relatively small interval of s (< 0) and then this separated zone is merged with the corner recirculating zone (type A_1 flow) before type B flow emerges as s is decreased. For co-rotating disk flows, flow types D and D_0 occur along the line $s = 1$ while type E_2 flow appears in a very narrow region in the vicinity of $(s, Re) = (0.99, 455)$.

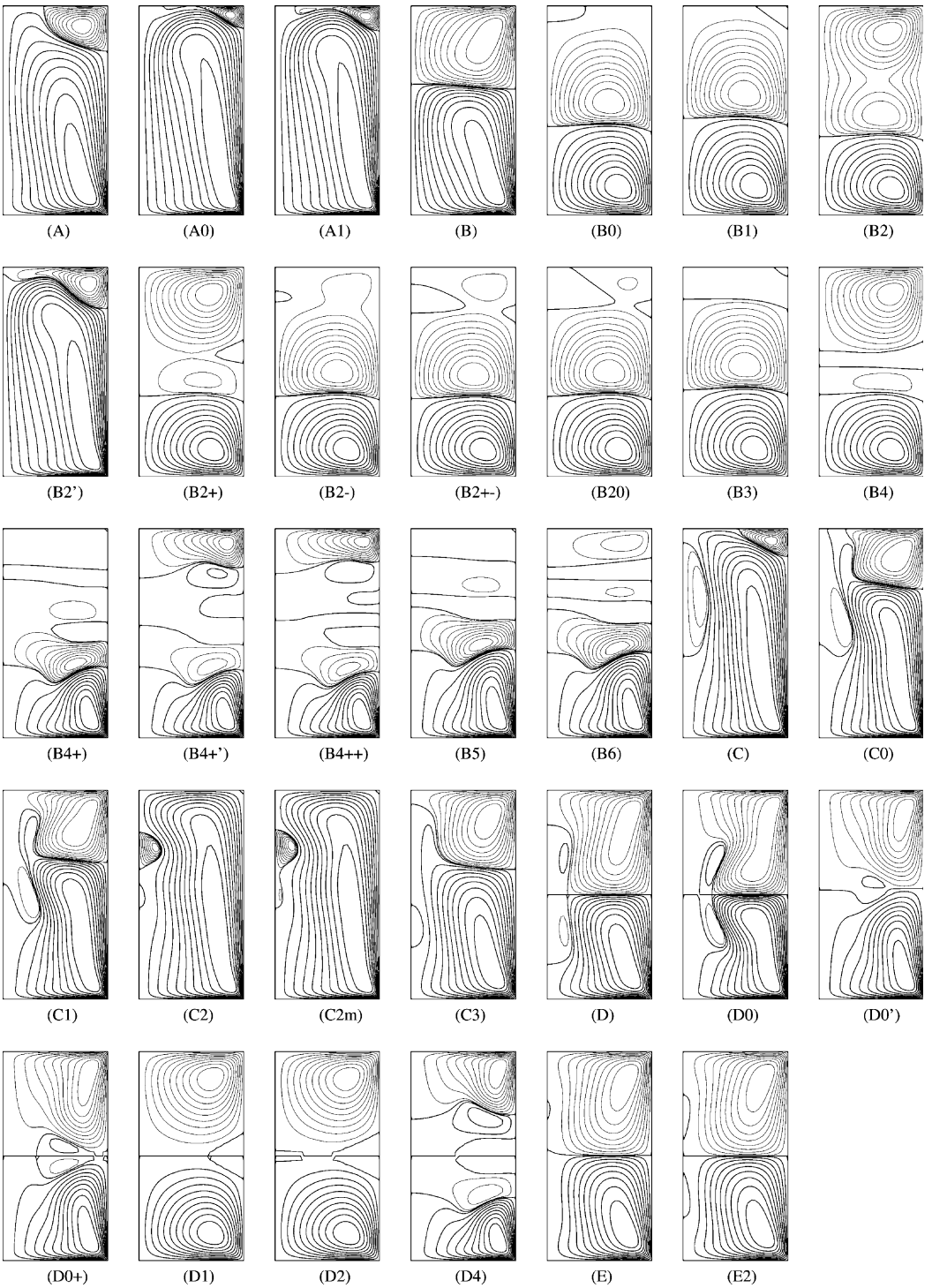

Fig. 2. List of meridional flow patterns. The values of (Re, s, Ri) are A $(700, 0.2, 0)$, A_0 $(1600, -0.22, 0)$, A_1 $(1600, -0.25, 0)$, B $(700, -0.6, 0)$, B_0 $(100, -0.025, 0.55)$, B_1 $(100, 0, 0.4125)$, B_2 $(100, -0.3, 0.9)$, $B_{2'}$ $(1600, -0.425, 0)$, B_{2+} $(100, 0.7, 0.9)$, B_{2-} $(100, 0.05, 0.8)$, B_{2+-} $(100, 0.05, 0.9)$, B_{20} $(100, -0.04, 0.8)$, B_3 $(100, 0.0125, 0.6)$, B_4 $(100, 0.9, 0.9)$, B_{4+} $(1000, 0, 0.9)$, $B_{4+'}$ $(1000, 0.6, 0.9)$, B_{4++} $(1000, 0.6, 1.0)$, B_5 $(1000, 0, 0.5)$, B_6 $(1000, -0.05, 0.55)$, C $(1600, 0.2, 0)$, C_0 $(1600, 0.475, 0)$, C_1 $(1600, 0.6, 0)$, C_2 $(1800, 0.002, 0)$, C_{2m} $(1800, 0.007, 0)$, C_3 $(700, 0.6, 0)$, D $(700, 1.0, 0)$, D_0 $(1600, 1.0, 0)$, $D_{0'}$ $(1000, 0.9, 0.15)$, D_{0+} $(1000, 1.0, 0.2)$, D_1 $(100, 1.0, 0.6)$, D_2 $(100, 1.0, 0.725)$, D_4 $(1000, 1.0, 0.9)$, E $(450, 0.99, 0)$ and E_2 $(460, 1.0, 0)$.

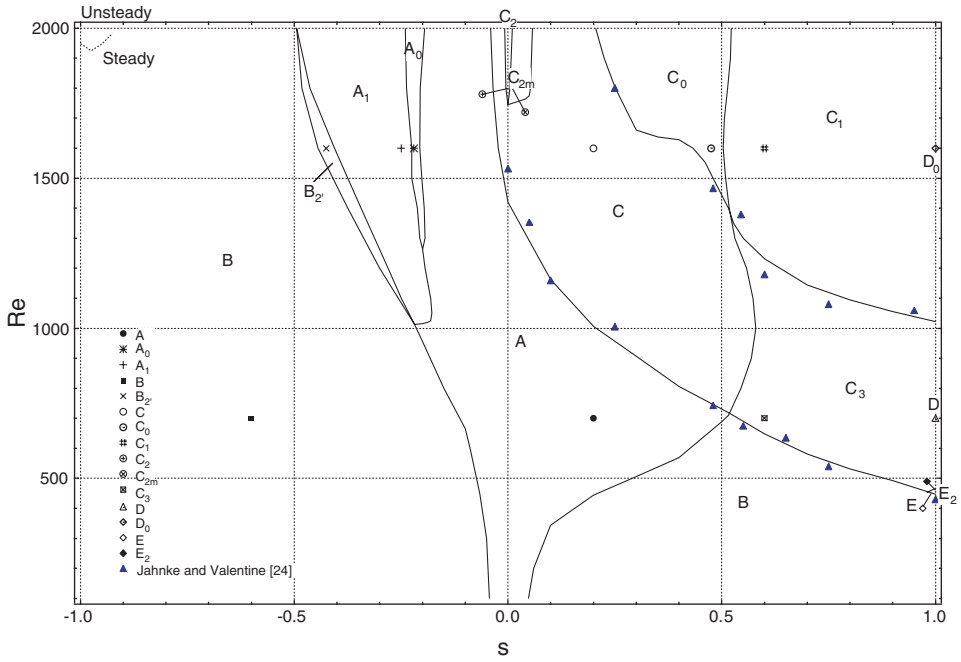

Fig. 3. Diagram of meridional flow patterns: $Ri = 0$.

Diagrams similar to the one presented in Fig. 3 are then constructed on (s, Ri) plane for flows with vertical temperature difference at two values of Re, $Re = 100$ and 1000 in Fig. 4. It is readily observed in these figures that the primary effect of vertical temperature difference on the flow pattern is to bring the meridional recirculation into vertically layered structures: Type A flow is replaced by a two-layered type B flow at $Ri = 0.0263$ for $Re = 100$ as Ri is increased. For $Re = 1000$, type A flow is altered to type B_2 flow at $Ri = 0.093$. The axis bubbles seen for $Re = 1000$ in flow types C and C_3 are eliminated under the influence of buoyancy at small values of Ri ($Ri \sim O(10^{-1})$). On the range of Ri considered in the present study, up to four layered recirculating zones (type B_4 flow) appear for $Re = 100$ and six such zones (type B_6) are noted for $Re = 1000$ depending on the value of s. For low Reynolds number flow at $Re = 100$, a considerable degree of similarity is noticed between the flows with s and $-s$ and this is reflected in the diagram: The diagram itself exhibits symmetry with respect to $s = 0$. As Re is increased, the symmetry is broken and the complexity of the diagram is increased. Even at $Re = 100$, the diagram contains narrow regions indicated as B_{2x} in Fig. 3(a) where four flow types appear and we are forced to be contended with mapping more obvious flow types, B_2, B_3 and B_4. Situation at $Re = 1000$ is intricate to the extent that the regions indicated as D_x and the regions indicated by dotted curves surrounding the region for B_5 contain several flow patterns.

3.2. Flow field and isotherms

When $Ri = 0$ and $s = 1.0$, top and bottom disks are rotating in the same direction with the same angular velocity (Fig. 5). Owing to the geometrical symmetry, the flow field and the isotherms are symmetric with respect to mid-height plane at $z = 1.0$. In the case of $s > 0$, fluid in the bulk of the cylinder exhibits quasi-rigid rotation with an intermediate angular velocity of both end disks. The Batchelor type flow is realized with the Ekman layer of thickness $O(Re^{-1/2})$ on both end disks and the Stewartson layer with double structure ($Re^{-1/4}$, $Re^{-1/3}$) on the sidewall (compare the boundary layer thickness in (a) and (c), e.g., for $s = 0$ in Fig. 5). Almost uniform axial flow appears in the vicinity of the rotating axis as a result of the Ekman suction. Mass efflux occurs on the slower rotating top disk and mass influx occurs on the faster rotating bottom disk. As the container is finite, main recirculation is induced in the meridional plane in order to compensate for the axial mass transfer. In the case of $s < 0$, i.e., the top and bottom disks are counter-rotating, shearing flow is created between the top and bottom boundaries. Recirculating zones are formed in the whole meridional section of the container. The angular momentum is transferred into the bulk fluid by the action of this secondary flow. When $s = -1$, the flow and temperature field is anti-symmetric with respect to the mid-height plane at $z = h/2$ (=1.0). For all the values of s at this Re, convection dominates the thermal transport and steep vertical temperature gradient is

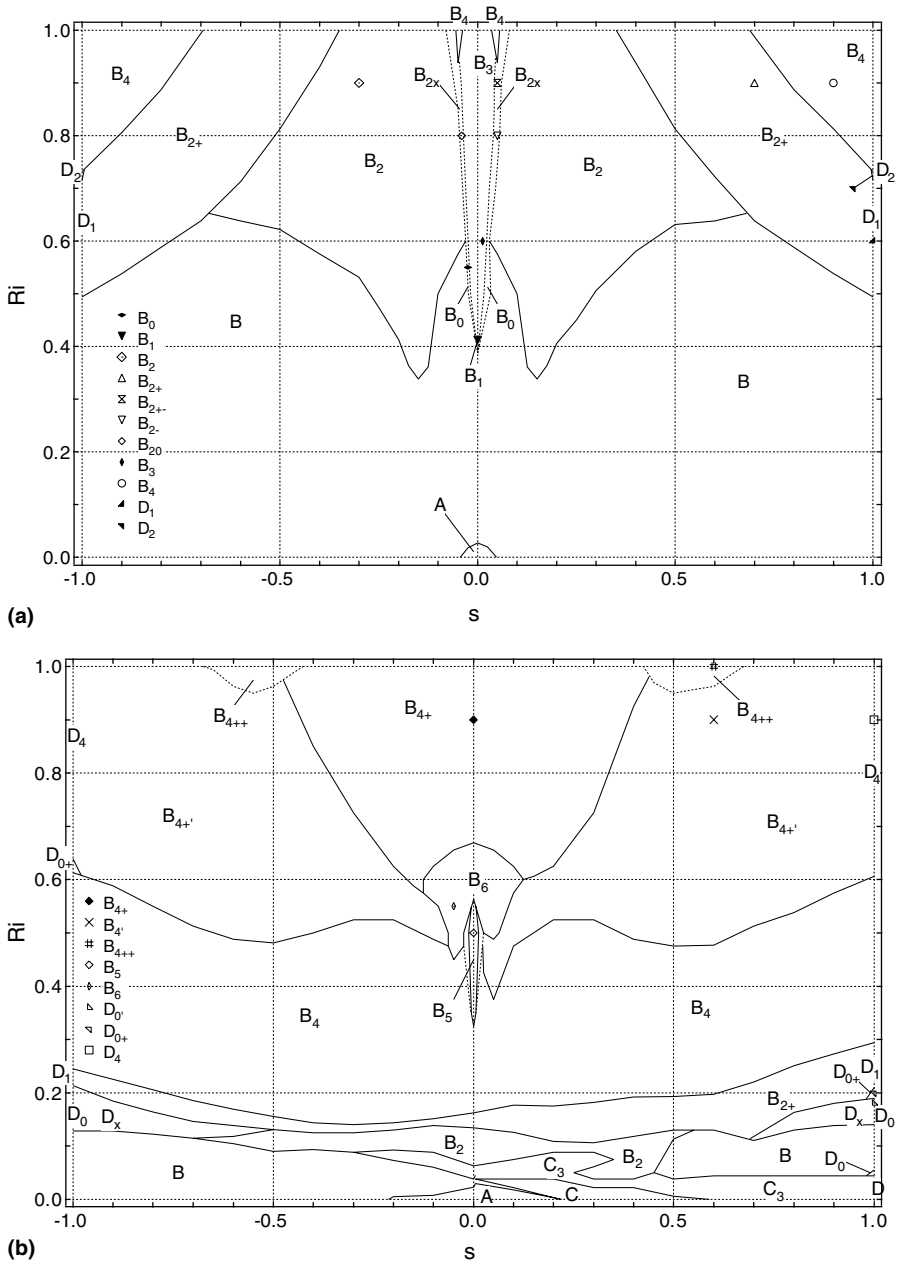

Fig. 4. Diagram of meridional flow patterns: (a) $Re = 100$ and (b) $Re = 1000$.

concentrated in the vicinity of the top and bottom boundaries. For $s = 1$ and -1, vertical temperature gradient is also noticed in the interior, on the radial outer portion ($0.5 < r$) of the mid-plane at $z = h/2$. Above observation on the flow between counter-rotating disks is qualitatively in accordance with the theoretical studies on homogeneous fluid [6] and this confirms our presumption as to the validity of the present numerical simulation.

The contour plots of streamfunction in Fig. 5(a) at $s = 1$ exhibit a pair of symmetric vortices attached to the axis of rotation and the mid-plane $z = h/2$. The behavior of these vortices as Re and h are varied with s fixed at $s = 1$ is well documented from the viewpoint of vortex breakdowns of homogeneous fluid in [20–23]. During the course of parametric study performed by the present authors, various vortex structures, e.g., toroidal, corner, axis vortices are noticed. Observation of these patterns as summarized in Fig. 3 displays an overall good agreement with the previous results for $s = 1$ and several new types are perceived for $s \neq 1$.

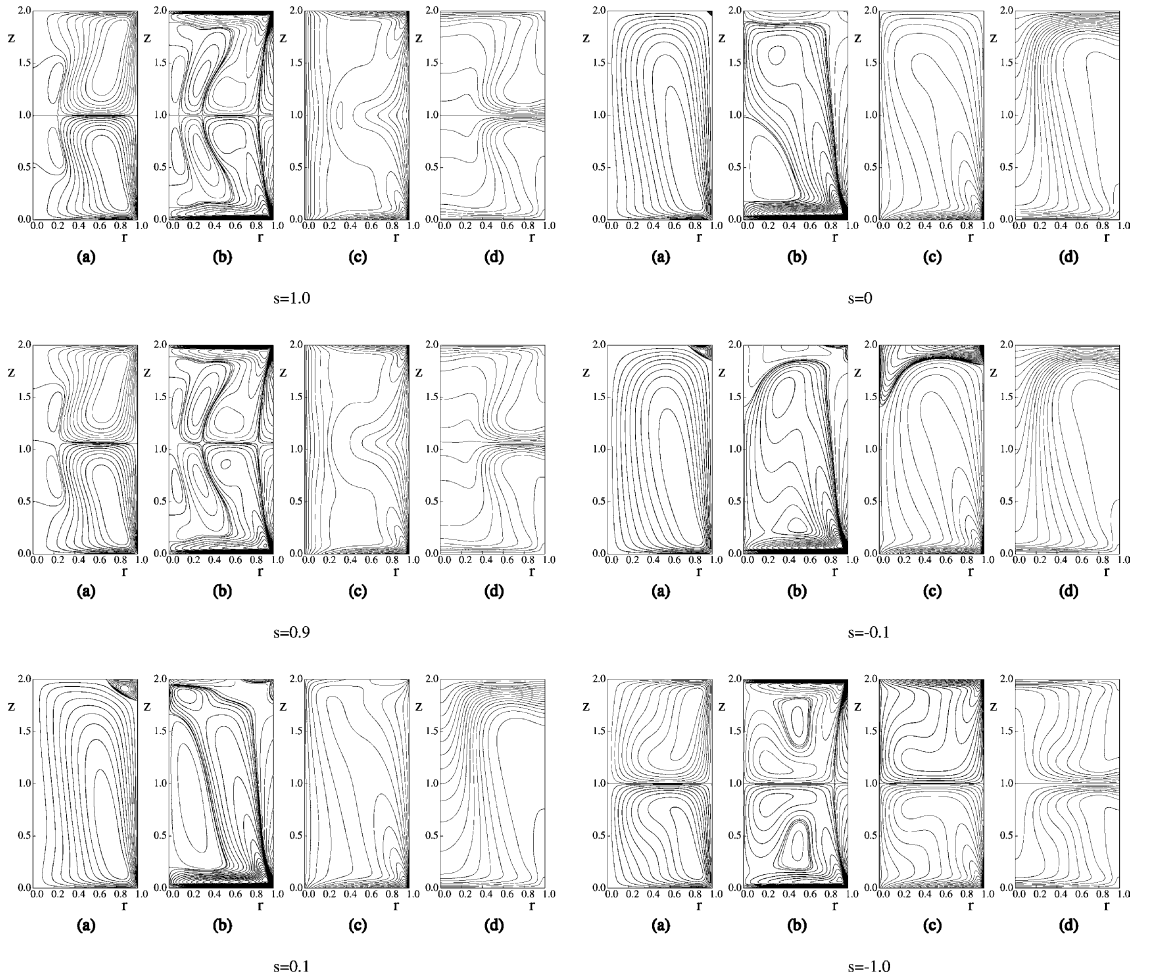

Fig. 5. Contour plots of (a) streamfunction, (b) azimuthal component of the vorticity, (c) azimuthal component of the velocity, and (d) isotherms. The value of contour lines are (a) $\psi = \psi_{\max}(i/10)^3$, $i = 0, 1, \ldots, 10$, $\psi_{\min}(i/10)^3$, $i = 1, \ldots, 10$; (b) $\omega = \omega_{\max}(i/10)^3$, $i = 0, 1, \ldots, 10$, $\omega = \omega_{\min}(i/10)^3$, $i = 1, \ldots, 10$; (c) $v = (i/10)^3$, $i = 0, 1, \ldots, 10$, $v = -(i/10)^3$, $i = 1, \ldots, 10$; and (d) $T = (i/20) - 0.5$, $i = 0, 1, \ldots, 20$, respectively. $Re = 1000$, $Pr = 1.0$ and $h = 2.0$; $Ri = 0$.

The physical mechanisms that induce these vortices are discussed in the previous literatures and the role of ω is stressed (e.g., [23]). The distribution of ω is determined as a solution of Eqs. (3)–(5) with the boundary condition including s as a variable. Consequently, it might be natural to expect various types of vortices not observed for flows with $s = 1$ configuration, because the value of s is not fixed to a single value and allowed to vary on an interval in the present configuration. Now the behavior of flow with large vertical temperature difference is described in the following at $Ri = 1.0$ for the same values of Re and s.

When $Ri = 1.0$ (Fig. 6), i.e., under the condition that temperature stratification is prominent, although the boundary layers are formed on both rotating disks, as a result of the inhibition of vertical motion by the buoyancy force, the Ekman suction disappears in the interior of the container (plots in (a) of Fig. 6). The suppression of meridional recirculation culminates in the loss of the mechanism that is responsible for the azimuthal momentum transfer (plots in (c) of Fig. 6) [14,15]. Fluid in the bulk apart from the rotating disks tends to be quiescent (note that the values of contour plots in Fig. 6(c) are not equi-divided between the maximum and minimum values). This behavior is in contrast to the previous case of $Ri = 0$ where the bulk fluid rotates with an intermediate angular velocity of the top and bottom disks. The connection between the top and bottom boundary layers is thus lost and the fluid in the vicinity of each disk rotates in each direction. The sidewall boundary layer is lost approximately from $z = 0.5$ to 1.5 in Fig. 6(b) when $s = 1.0$, 0.9 and -1.0. As clearly shown in the isotherms, the temperature distribution is dominated by the conductive heat transfer.

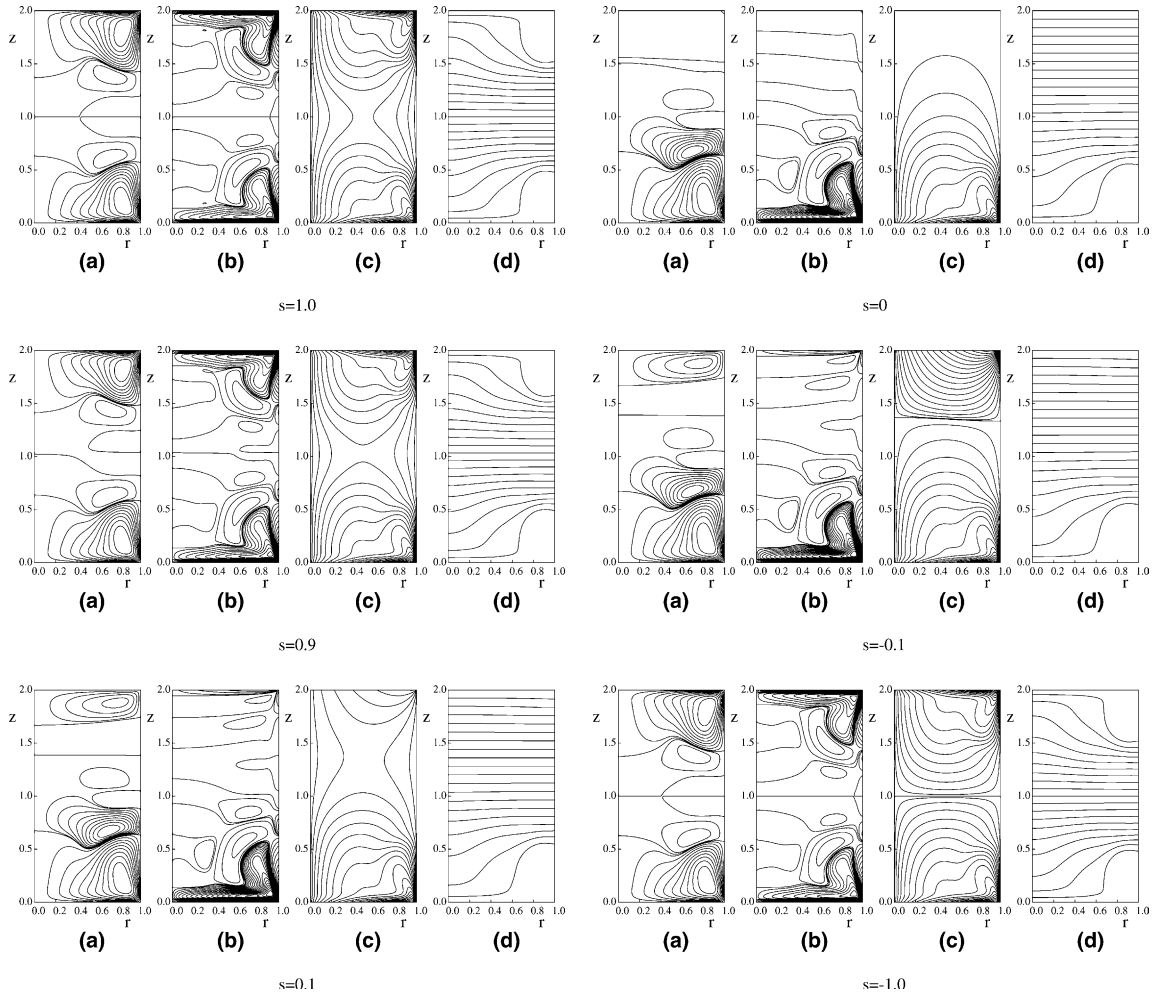

Fig. 6. Similar plots to Fig. 2. $Re = 1000$, $Pr = 1.0$ and $h = 2.0$; $Ri = 1.0$.

3.3. Velocity distribution

In order to study the vertical structure of the flows in detail, each component of the velocity and the temperature are plotted along a vertical line at $r = 0.8$ for $Ri = 0$, 1.0 and representative values of s in Fig. 7. The prohibition of the vertical motion under the stratification condition and the conduction dominated linear temperature distribution is observed in Fig. 7 as in Figs. 5 and 6.

The difference of rotating flows with and without temperature stratification is displayed in a marked manner when the value of rotation ratio s is close to unity. When $s \cong 1.0$ and Re is sufficiently high, much of the fluid in the cylinder accomplishes quasi-rigid rotation. In such a case, adoption of Rossby number Ro and the Ekman number Ek based on the rotating frame fixed to quasi-rigidly rotating fluid might be more convenient for describing the flow behavior. Fig. 8 shows the absolute value of the velocity components $|u|$ and $|w|$ at an arbitrarily chosen point at $(r,z) = (0.3, h/2)$ plotted as functions of Ek. If Ro and Ek are both small quantities, appropriate scaling for the inner flow of homogeneous fluid ($S = 0$) is $u \sim \mathrm{O}(Ek)$ and $w \sim \mathrm{O}(Ek^{1/2})$ [25]. Under the stratification condition ($S > 0$), the scaling for inner flow is $w \sim \mathrm{O}(Ek/Pr\,S)$. Plots in Fig. 8 indicate that theoretical scaling holds as an approximation even at $Ro = 0.1$ for the present flow configuration. These plots in Figs. 7 and 8 clearly indicate the qualitative difference between the rotating flow of homogeneous fluid and under stratification.

3.4. Nusselt number

The difference in the flow behavior of homogeneous fluid and that under thermal stratification is fully described above for the present flow configuration. We

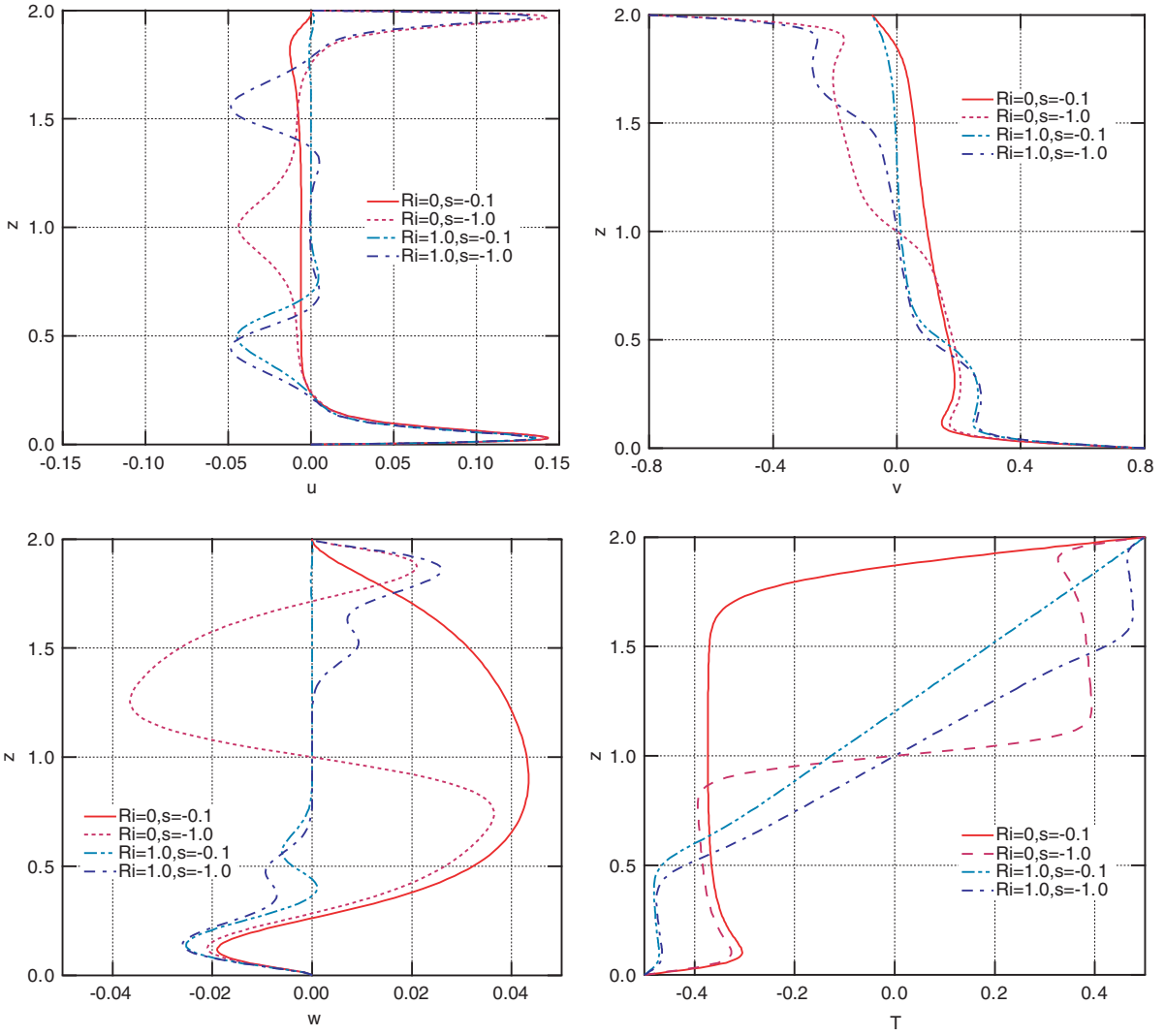

Fig. 7. Velocity and temperature distribution along a vertical line at $r = 0.8$. $Re = 1000$, $Pr = 1.0$ and $h = 2.0$.

would move on to study the effect of vertical temperature difference on the heat transfer in the following. As the cylinder sidewall is thermally insulated, heat is transferred from the top hot disk at $z = h$ to the bottom cold disk at $z = 0$. The local Nusselt number at both disks and the average Nusselt number $\overline{Nu}$ are defined, respectively, as follows:

$$Nu(r) = \left.\frac{\partial T}{\partial z}\right|_{z=0 \text{ or } z=h}, \tag{7}$$

$$\overline{Nu} = \frac{1}{\pi}\int_0^{2\pi}\int_0^1 \frac{\partial T}{\partial z} r\,\mathrm{d}r\,\mathrm{d}\theta. \tag{8}$$

The local Nusselt number at the top and bottom disks for several values of rotation ratio s is plotted in Fig. 9 for $Ri = 0$ and in Fig. 10 for $Ri = 1.0$, respectively. When $Ri = 0$ and $s = 0.1$, 0, -0.1 and -1.0 (see Fig. 9), the local Nusselt number on the bottom disk attains local maximum at $r = 0$ and decreases as r is increased toward the sidewall located at $r = 1.0$. The Nusselt number on the top disk reaches its extreme value at approximately $r = 0.7$ except for $s = -1.0$ due to the convectional heat transfer caused by the meridional recirculation. When $s = -1.0$, owing to the vertical shearing flow, the value of the Nusselt number is largest at $r = 0$. When $Ri = 1.0$ (see Fig. 10), the conduction dominates the vertical heat transfer and the local Nusselt number approaches to an almost constant value. This tendency is most conspicuous at the top disk with $s \cong 0$. For all the values of s computed, local Nusselt number is largest at $r = 0$ and decreases as r is increased toward sidewall when $Ri = 1.0$. Also noted in Fig. 10 is

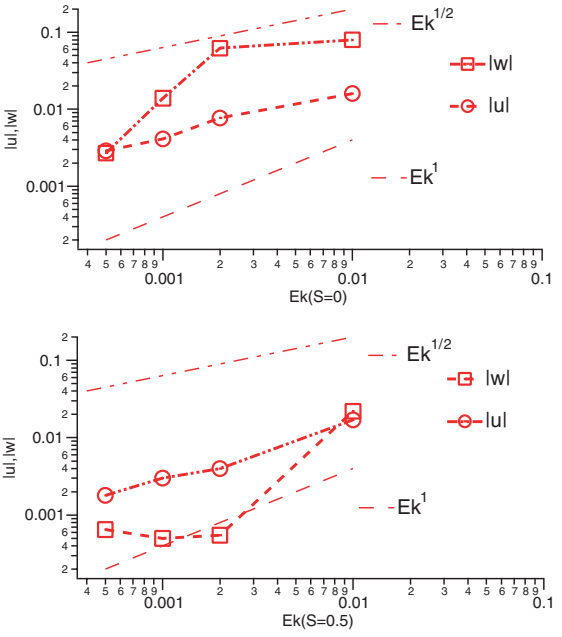

Fig. 8. Plots of velocity component $|u|$ and $|w|$ at a point $(r,z)=(0.3,h/2)$ vs. Ek. $Ro=0.1$. Stratification parameter $S=0$ and 0.5. $Pr=1.0$, $h=2.0$.

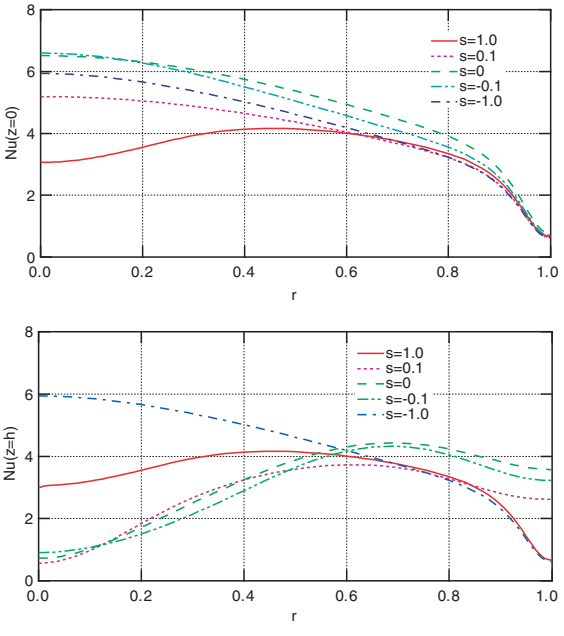

Fig. 9. Local Nusselt number vs. $Re=1000$, $Pr=1.0$ and $h=2.0$; $Ri=0$.

that plots for $s=1.0$ and -1.0 are almost identical. Plots for $s=0.1$, 0 and -0.1 are likewise barely distinguishable with each other.

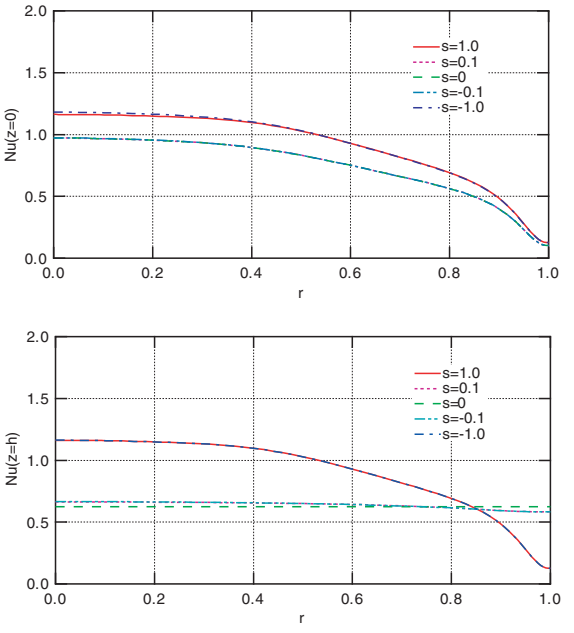

Fig. 10. Similar plots to Fig. 6. $Re=1000$, $Pr=1.0$ and $h=2.0$; $Ri=1.0$.

The average Nusselt number is plotted next as a function of Ri in Fig. 11, as a function of rotation ratio s in Fig. 12 and as a function of Re in Fig. 13, respectively. As Ri is increased to O(1) values, the average Nusselt number $\overline{Nu}$ for all the values of s approaches the reciprocal of the aspect ratio, i.e., $1/h$ (=0.5 in the present case at $h=2.0$ as R is chosen as the reference scale for the length) which is the value of the conduction limit (see Fig. 11). For the range of Re and s studied, it appears that $\overline{Nu}$ achieves extreme value at $s=-1.0$ when $Ri=0$ and $Re\leqslant 1000$ (see Fig. 12(a)). When $Ri=0$, $Re=1500$ and 2000, $\overline{Nu}$ takes extreme value in the vicinity of $s=-0.075$. By referring to Fig. 3, it is noticed that the maximum value of $\overline{Nu}$ is attained when a single main recirculation is created in the meridional plane (flow

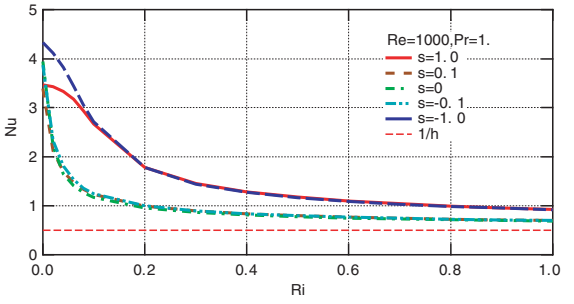

Fig. 11. Average Nusselt number vs. Ri. $Re=1000$, $Pr=1.0$ and $h=2.0$.

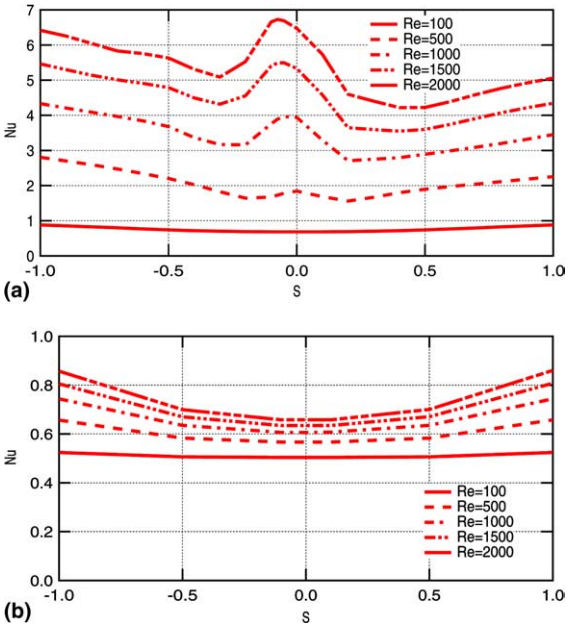

Fig. 12. Average Nusselt number vs. rotation ratio s: (a) $Ri = 0$ and (b) $Ri = 1.0$. $Pr = 1.0$ and $h = 2.0$.

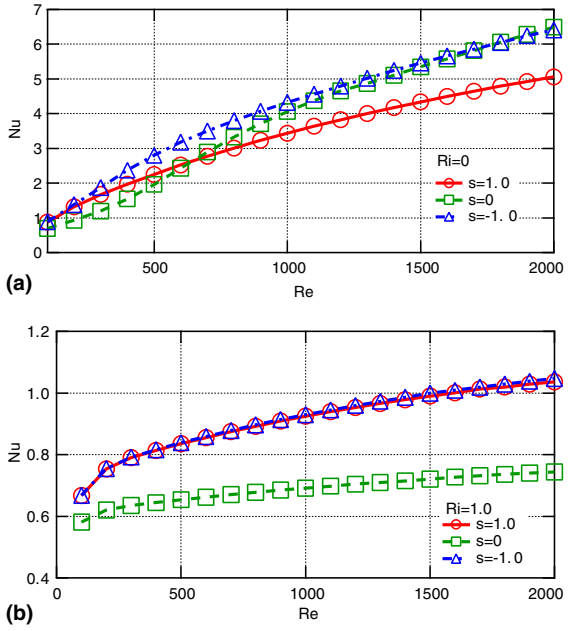

Fig. 13. Average Nusselt number vs. Re. (a) $Ri = 0$, (b) $Ri = 1.0$. $Pr = 1.0$ and $h = 2.0$.

type A) for these high Re flows. Under the stratification condition ($Ri = 1.0$), $\overline{Nu}$ exhibits an almost flat curve which exposes considerable degree of symmetry with respect to $s = 0$, with local minimum located at $s = 0$ (Fig. 12(a)). By comparing the plots in Fig. 6 for $s = 1.0$ and -1.0, the similarity of isotherms and even the velocity contours is amazingly noted if we remember the fact that in the former, the end disks are co-rotating and in the latter, they are counter-rotating. Also the plots of local Nusselt number for $s = 1.0$ and -1.0 in Fig. 10 are almost identical as mentioned above. In accordance with these observations, $\overline{Nu}$ for $s = 1.0$ and -1.0 take very close values as shown in Fig. 12. Under the temperature stratification, weakened Ekman suction results in stationary bulk fluid. With the bulk fluid at rest, the boundary layers on the end of the disks are not influenced by each other. This means that whether the disks are co-rotating or counter-rotating, it does not affect the thickness of the boundary layers. This discussion leads us to a conclusion that when $Ri \gg 1$, the average Nusselt number for s is almost equal to the average Nusselt number for $-s$. In other words, under strong temperature stratification, the value of $\overline{Nu}$ for co-rotating disks with rotation ratio s is almost equal to the value of $\overline{Nu}$ for counter-rotating disks with rotation ratio $-s$. The average Nusselt number plotted as a function of Re in Fig. 13 displays that $\overline{Nu}$ is an increasing function of Re and the correlation $Re^{1/2}$ holds as an appropriation when $s = 1$ and $Ri = 0$. For $s = 0, -1$ and $Ri = 0$, a slight variation from $Re^{1/2}$ is noted in $\overline{Nu}$ for the range of parameters studied.

4. Summary

The flows in cylindrical container with co-/counter-rotating end disks with stationary sidewall are numerically studied within the axisymmetric parameter range. The effect of the buoyancy under thermally stable boundary condition is examined for the flows between two disks when $Re \gg 1$, $Pr = O(1)$ and $h = O(1)$. When the buoyancy effect is negligible and the disks are co-rotating, the bulk fluid rotates with an intermediate angular velocity of the end disks with the boundary layers formed on all the boundaries. When the disks are counter-rotating, azimuthal shear flow with meridional recirculating secondary flow is created. Under the temperature stratification condition, owing to the inhibition of the vertical motion by the buoyancy, the Ekman suction is lost and the sidewall boundary layer disappears. The bulk flow approaches to the state of rest, leaving the fluid in the vicinity of each end disk rotating in each direction. These observations are in qualitative agreement with the classical theoretical predictions [2,14,15]. The secondary flow exhibits various types of recirculating zones and these flow patterns are presented in the form of diagrams on the parameter planes. For the range of rotation ratio s studied, the average Nusselt number achieves maximum value at $s = -1$ for low Re flows and maximum value is attained in the vicinity of

$s = 0$ for high Re flows, respectively, when $Ri = 0$. On the contrary, when $Ri = O(1)$, the average Nusselt number appears as almost constant but an increasing function of $|s|$. It is argued that when $Ri \gg 1$, the average Nusselt number as a function of s is almost symmetric with respect to $s = 0$ due to the suppressed Ekman suction. It might be suggested from the present numerical simulation that the adoption of vertically stable temperature difference provides a technological means to control the rotation of inner fluid confined in containers with rotating end disks. For the situations in which non-rotating bulk fluid is preferable, the imposition of vertical large temperature difference provides a means to realize the desired flow in the container with both end disks are rotating.

Acknowledgements

The authors are grateful to the anonymous reviewers whose comments and suggestions led to the improvement of the revised manuscript. Part of the computer jobs in the parametric study were submitted by Taichi Tomine. The authors thank his contribution.

References

[1] Th.v. Kármán, Über laminare und turbulente Reibung, Zeitshr. Angew. Math. Mech. 1 (4) (1921) 233–252.
[2] G.K. Batchelor, Note on a class of solutions of the Navier–Stokes equations representing steady rotationally-symmetric flow, Quart. J. Mech. 1 (1951) 29–41.
[3] K. Stewartson, On the flow between two rotating coaxial disks, Proc. Camb. Phil. Soc. 49 (1953) 333–341.
[4] L.v. Wijngaarden, On multiple solutions and other phenomena in rotating fluids, Fluid Dynam. Trans. 12 (1985) 157–179.
[5] P.J. Zandbergen, D. Dijkstra, Von Kármán swirling flows, Ann. Rev. Fluid Mech. 19 (1987) 465–491.
[6] A. Delgado, On the rotationally symmetric laminar flow of Newtonian fluids induced by rotating disks, in: C. Egbers, G. Pfster (Eds.), Physics of Rotating Fluids, Springer, Berlin, 2000, pp. 417–439.
[7] Y. Jaluria, Fluid flow phenomena in materials processing—the 2000 Freeman scholar lecture, Trans. ASME: J. Fluids Eng. 123 (2001) 173–210.
[8] V. Prasad, H. Zhang, A.P. Anselmo, Transport phenomena in Czochralski crystal growth processes, in: G.A. Greene (Ed.), Advances in Heat Transfer, vol. 30, Academic Press, London, 1997, pp. 313–435.
[9] D. Dijkstra, G.J.F.V. Heijst, The flow between two finite rotating disks enclosed by a cylinder, J. Fluid Mech. 128 (1983) 123–154.
[10] J. Sanches, F. Marques, J.M. Lopez, A continuation and bifurcation technique for Navier–Stokes flows, J. Comput. Phys. 180 (2002) 78–98.
[11] J.M. Lopez, Characteristics of endwall and sidewall boundary layers in a rotating cylinder with a differentially rotating endwall, J. Fluid. Mech. 359 (1998) 49–79.
[12] A.Y. Gelfgat, P.Z. Bar-Yoseph, A. Solan, Steady states and oscillatory instability of swirling flow in cylinder with rotating top and bottom, Phys. Fluids. 8 (10) (1996) 2614–2625.
[13] A.Y. Gelfgat, P.Z. Bar-Yoseph, A. Solan, Confined swirling flow simulation using spectral Galerkin and finite volume methods, in: Proc. ASME Fluids Engineering Division Summer Meeting, FED-vol. 238, 1996, pp. 105–112.
[14] V. Barcilon, J. Pedlosky, Linear theory of rotating stratified fluid motions, J. Fluid Mech. 29 (1967) 1–16.
[15] V. Barcilon, J. Pedlosky, On the steady motions produced by a stable stratification in a rapidly rotating fluid, J. Fluid Mech. 29 (1967) 673–690.
[16] W.N. Kim, J.M. Hyun, Convective heat transfer in a cylinder with a rotating lid stable stratification, Int. J. Heat Fluid Flow 18 (1997) 384–388.
[17] C.H. Lee, J.M. Hyun, Flow of a stratified fluid in a cylinder with a rotating lid, Int. J. Heat Fluid Flow 20 (1999) 26–33.
[18] R. Iwatsu, Flow pattern and heat transfer of swirling flows in cylindrical container with rotating top and stable temperature gradient, Int. J. Heat Mass Trans. 47 (2004) 2755–2765.
[19] R. Iwatsu, A second-order axisymmetric flow solver on cylindrical coordinate system, Compt. Fluid Dynam. J. 12 (4) (2004) 595–600.
[20] D.T. Valentine, C.C. Jahnke, Flows induced in a cylinder with both end walls rotating, Phys. Fluids 6 (8) (1994) 2702–2710.
[21] M. Brons, L.K. Voigt, J.N. Sorensen, Topology of vortex breakdown bubbles in a cylinder with a rotating bottom and a free surface, J. Fluid Mech. 428 (2001) 133–148.
[22] R. Iwatsu, Numerical study of flows in a cylindrical container with rotating bottom and top flat free surface, J. Phys. Soc. Jpn. 74 (1) (2005) 333–344.
[23] C.C. Jahnke, D.T. Valentine, Recirculation zones in a cylindrical container, Trans. ASME: J. Fluid Eng. 120 (1998) 680–684.
[24] K.G. Roesner, Recirculation zones in a cylinder with rotating lid, in: H.K. Moffatt, A. Tsinober (Eds.), Topological Fluid Mechanics, Proc. IUTAM Symposium, Cambridge University Press, Cambridge, 1990, pp. 699–708.
[25] P.F. Linden, The flow of a stratified fluid in a rotating annulus, J. Fluid Mech. 79 (1977) 435–447.